Supplementary Information

Joint Subarray Acoustic Tweezers

Enable Controllable Cell Translation, Rotation, and Deformation

Liang Shen[1,2], Zhenhua Tian[2,*], Kaichun Yang[1], Joseph Rich[3], Jianping Xia[1], Neil Upreti[1], Jinxin Zhang[1], Chuyi Chen[1], Nanjing Hao[1], Zhichao Pei[1], Tony Jun Huang[1,*]

[1]Department of Mechanical Engineering and Materials Science, Duke University, Durham, NC, 27708, USA

[2]Department of Mechanical Engineering, Virginia Polytechnical Institute and State University, Blacksburg, VA, 24061, USA

[3]Department of Biomedical Engineering, Duke University, Durham, NC, 27708, USA

[*] Corresponding author: Z. T. (tianz@vt.edu), T.H. (tony.huang@duke.edu)

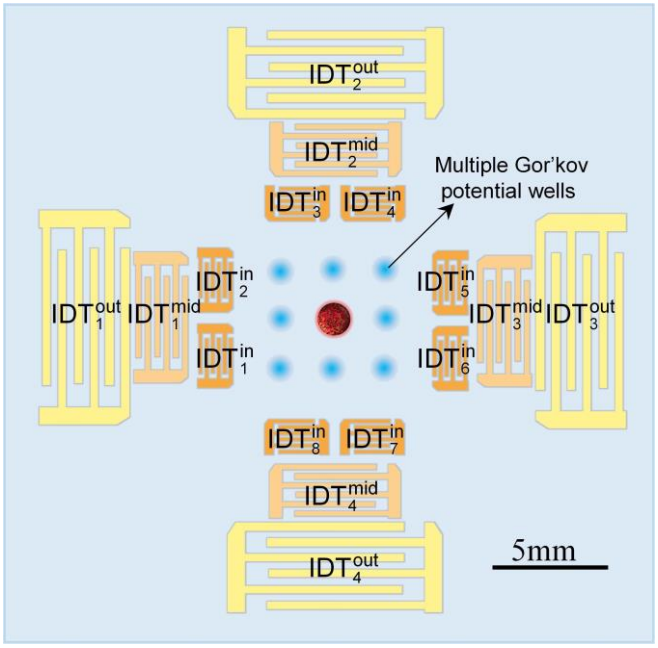

Supplementary Figure 1. Schematic of an IDT array designed for the Joint Subarray Acoustic Tweezers (JSAT) platform. The IDT array is composed of outer, middle, and inner subarrays with 4, 4, and 8 IDTs, respectively. The IDTs in these subarrays are labeled with distinct superscripts "out", "mid", and "in", respectively. For the IDTs in each subarray, the subscript represents the element index. Multiple Gor'kov potential wells (*i.e.*, 3×3 potential wells illustrated by blue spots) can be generated in a microfluidic chamber at the array center when all the outer IDTs are excited to trap cells. For example, a cell (illustrated by a red sphere) is trapped at the center well of a 3×3 well array.

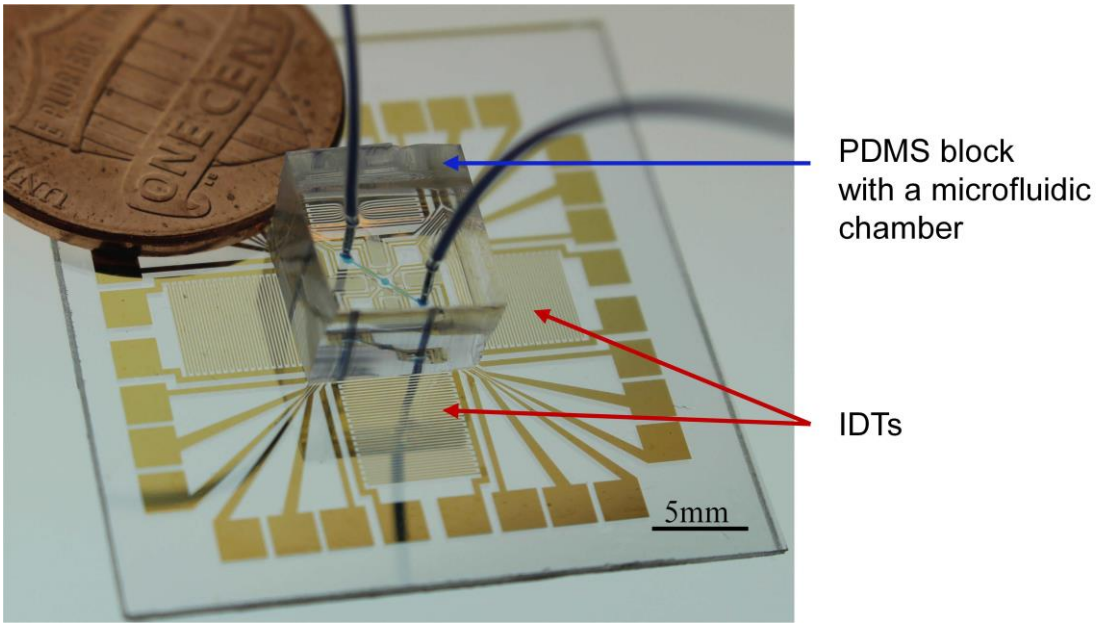

Supplementary Figure 2. A photo of a fabricated JSAT device. The device is composed of a PDMS block containing a microfluidic chamber and an IDT array with three subarrays deposited on a Y128-cut $LiNbO_3$ substrate.

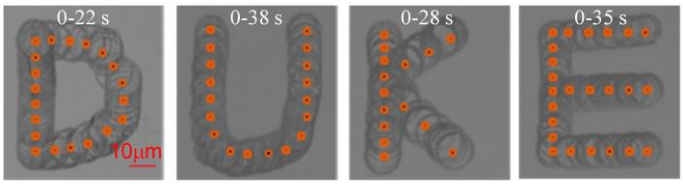

Supplementary Figure 3. Comparisons between actual and predicted cell positions for four cases of translating a cell to depict 'D,' 'U,' 'K,' and 'E' *via* JSAT. For each case, images are extracted from a recoded video and then stacked. Each stacked image is overlayed with orange dots, representing positions predicted by the phase modulation-based translation approach. Scale bar: 10 μm.

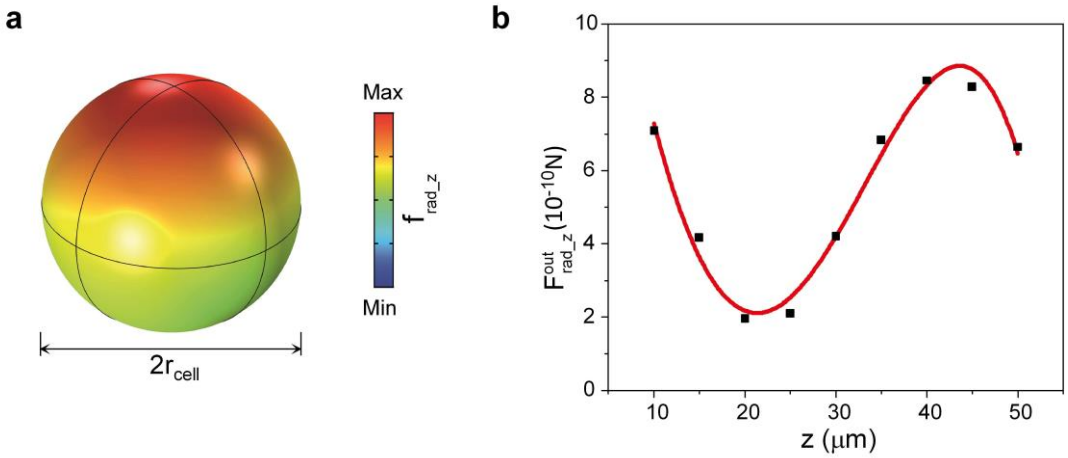

Supplementary Figure 4. Simulated acoustic radiation force in the *z*-direction. (**a**) Simulated acoustic radiation force (in the *z*-direction) field when all the IDTs of the outer subarray are on. The force is obtained following the approach in Supplementary Note 1. (**b**) Simulated acoustic radiation forces (in the *z*-direction) for a cell located at different *z* positions. The black dots represent data points from simulations. The red curve is obtained through curve fitting with the simulation data. For these simulations, the cell radius r_{cell} is set to 7.5 μm.

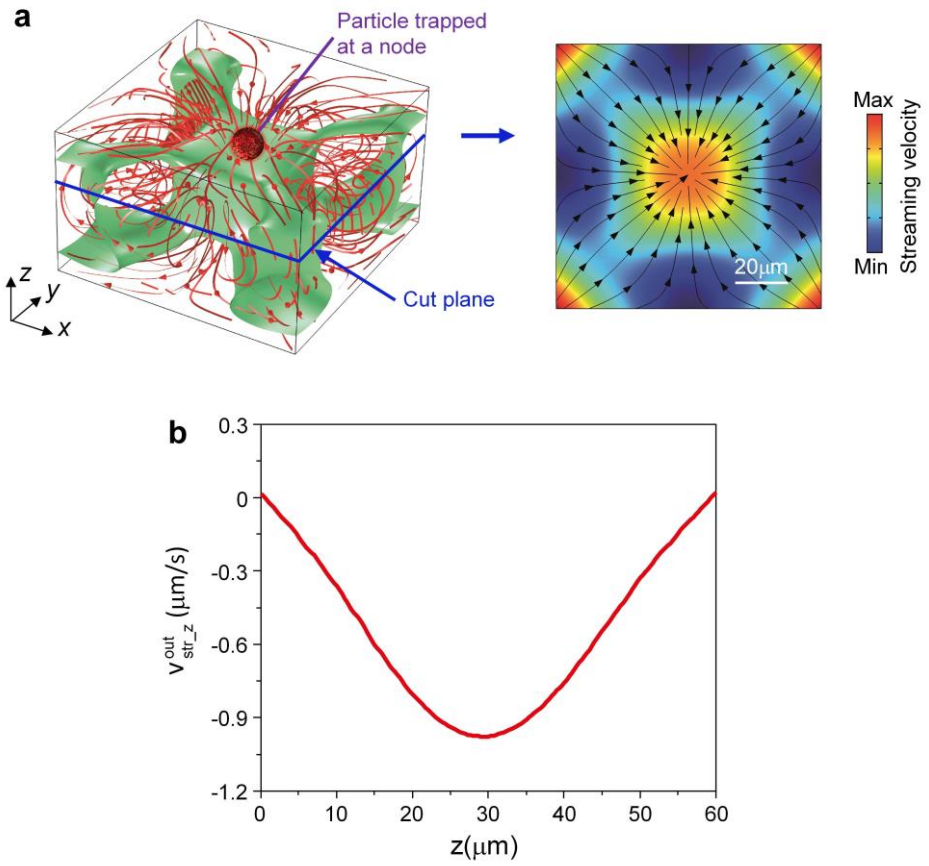

Supplementary Figure 5. Simulation results of acoustic streaming generated by the outer IDT subarray. (**a**, left) Simulated streamlines (3D view) showing that acoustic streaming flows down at the pressure node (the center of the simulation domain), then flows to pressure antinodes (four corners of the simulation domain), after that flows upward, and finally moves to the pressure node. The green 3D surface represents a constant streaming velocity surface, which is symmetric with respect to both the *x*- and *y*-axes. (**a**, right) A 2D view of the simulated acoustic streaming field showing the streaming velocity distribution in a cut plane illustrated in (**a**, left). (**b**) Simulated streaming velocity (z-component) at the pressure node versus *z* position.

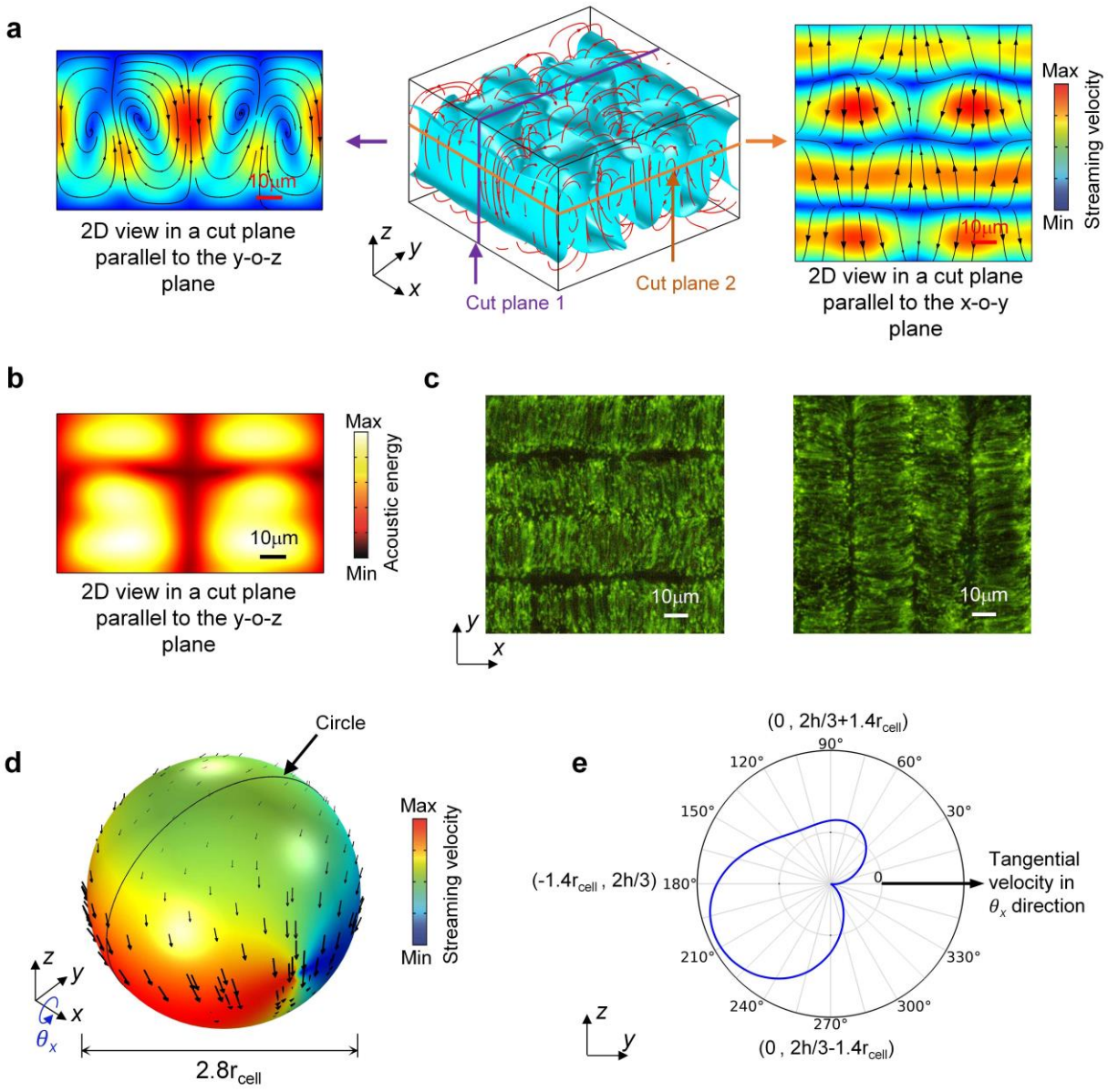

Supplementary Figure 6. Simulation and experiment results for understanding the mechanism of rotating a cell in the θ_x- and θ_y- directions. (**a**, middle) Simulated streamlines (3D view) showing four vortices carrying angular momentum vectors in $\pm x$- directions generated by IDT_2^{mid} and IDT_4^{mid} with excitation voltages in a relation of 1:0.8. (**a**, left) A 2D view of the simulated streaming field in cut plane 1 showing counter-chirality streaming vortices at different sides of a pressure node at the center of the simulation domain. (**a**, right) A 2D view of the simulated streaming field in the cut plane 2. (**b**) A 2D view of the simulated acoustic energy field in the cut plane 1. (**c**) Stacked images of 200 nm fluorescent tracing particles whose motions were dominantly driven by streaming vortices generated by IDT_2^{mid} and IDT_4^{mid} (left) and IDT_1^{mid} and IDT_3^{mid} (right). (**d**) Simulated streaming velocity distribution on the surface of a sphere with a diameter of 2.8×r_{cell}. For this simulation, the cell radius r_{cell} was set to 7.5 μm. The cell's surface was considered as a no-slipping boundary. The cell center

was at a position of (x, y, z)=(0, 0, 2h/3). The microfluidic chamber's height h was set to 60 μm. (**e**) Simulated tangential velocity distribution along a circle with x =0 μm on the sphere in (**d**). This distribution shows that tangential velocities leading to cell rotation in the $+\theta_x$-direction are dominant.

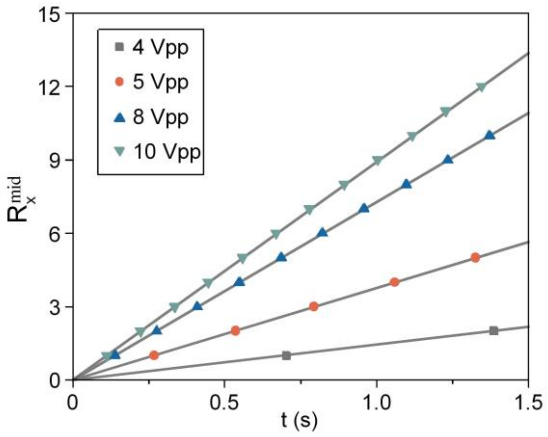

Supplementary Figure 7. Experientially observed cell revolutions for cases with different input voltages. The markers of different shapes are experimental results. The solid lines are linear fitting results. The experimental results follow good linear trends, indicating the ability to achieve stable cell rotation at different input voltages.

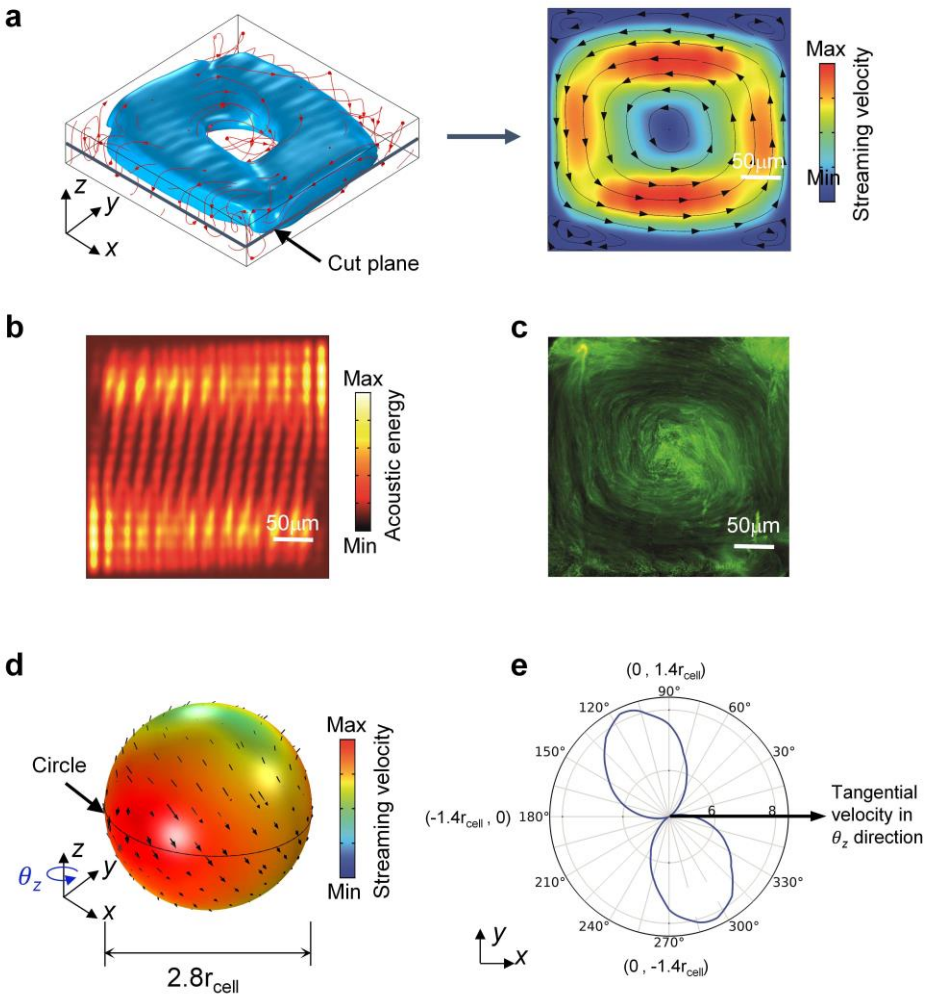

Supplementary Figure 8. Simulation and experiment results for understanding the mechanism of rotating a cell in the θ_z-direction. (**a**, left) Simulated streamlines (3D view) of an acoustic streaming vortex induced by traveling SAWs generated by IDT_1^{in} and IDT_5^{in}. (**a**, right) A 2D view of the simulated streaming field in a cut plane showing a streaming vortex with streamlines dominantly in the $+\theta_z$-direction. (**b**) A 2D view of the simulated acoustic energy field in the cut plane from (**a**, left). (**c**) Stacked images of 200 nm fluorescent tracing particles whose motions were dominantly driven by a streaming vortex generated by IDT_1^{in} and IDT_5^{in}. (**d**) Simulated streaming velocity distribution on the surface of a sphere with a diameter of $2.8\times r_{cell}$. For this simulation, the cell radius r_{cell} was set to 7.5 μm. The cell's surface was considered as a no-slipping boundary. The cell center was at a position of $(x, y, z)=(0, 0, 2h/3)$. The microfluidic chamber's height h was set to 60 μm. (**e**) Simulated tangential velocity distribution along a circle with $z=2h/3$ on the sphere illustrated in (**d**). This distribution shows that tangential velocities that can lead to cell rotation in the $+\theta_z$-direction are dominant.

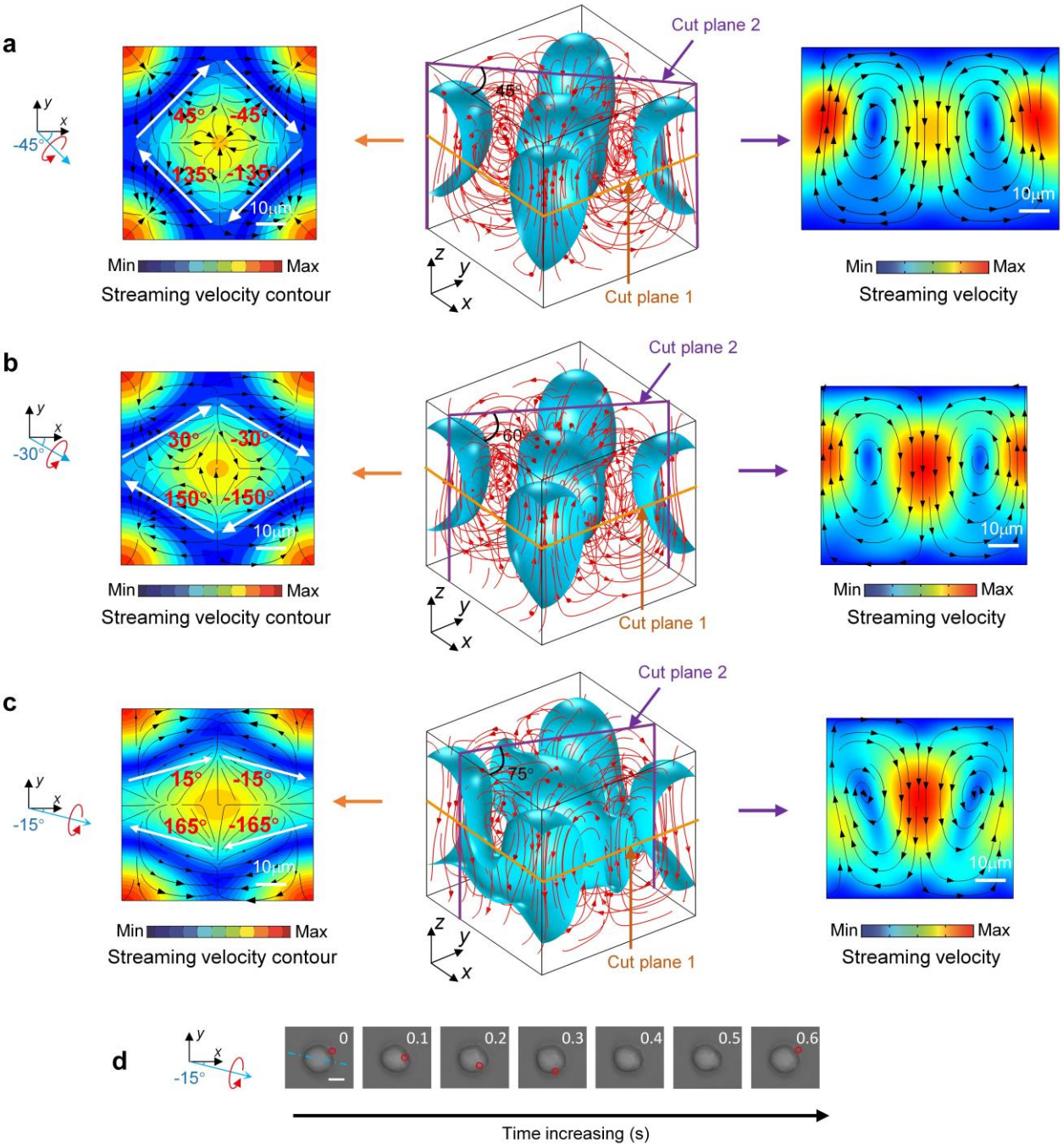

Supplementary Figure 9. Numerical and experimental results for understanding the mechanism of rotating a cell with respect to an axis that can be steered. (**a**) Simulated acoustic streaming fields (middle: 3D view, left: 2D view in the cut plane 1, right: 2D view in the cut plane 2), when amplitudes of standing SAWs along the *x*- and *y*-axes are the same. The *x*-axis (or *y*-axis) standing SAWs are generated by IDT_1^{mid} and IDT_3^{mid} (or IDT_2^{mid} and IDT_4^{mid}). The streaming field shows four streaming vortexes with upward streamlines at pressure antinodes (at the four corners of the simulation domain) and downward streamlines at a pressure node (at the domain center). The angular momentum vectors of these four vortices are in -45°, 45°, 135° and -135° with respect to the +*x*-direction. (**b**) Simulated acoustic streaming fields (middle: 3D view, left: 2D view in the cut plane 1,

right: 2D view in the cut plane 2), when the amplitude of *x*-axis standing SAWs and the amplitude of *y*-axis standing SAWs have a ratio of 0.57:1. The angular momentum vectors of the four vortices are pointing to -30°, 30°, 150° and -150° with respect to +*x*-direction. (**c**) Simulated acoustic streaming fields (middle: 3D view, left: 2D view in the cut plane 1, right: 2D view in the cut plane 2), when the amplitude of *x*-axis standing SAWs and the amplitude of *y*-axis standing SAWs have a ratio of 0.3:1. The angular momentum vectors of the four vortices are pointing to -15°, 15°, 165° and -165° with respect to +*x*-direction. (**d**) Time-sequential images showing that an MCF7 cell positioned at $x=\lambda^{mid}/2$ and $y=\lambda^{mid}/2$ was rotated with respect to an axis in the −15° in the *x*-*y* plane. Scale bar: 10 μm.

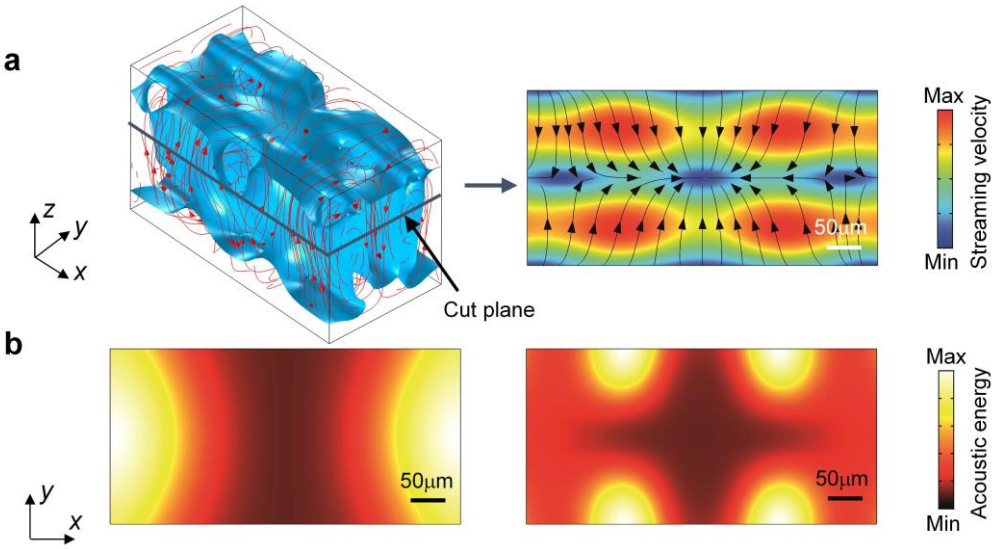

Supplementary Figure 10. Simulation results for understanding the mechanism of simultaneously translating a cell in the *x*-direction, as well as rotating the cell in the θ_x-direction. (**a**) Simulated acoustic streaming fields (left: 3D view, right: 2D view in the cut plane), when activating IDT_1^{out} and IDT_3^{out} to generate low-frequency *x*-axis standing SAWs, as well as IDT_2^{mid} and IDT_4^{mid} to generate high-frequency *y*-axis standing SAWs. The streaming field shows streaming vortices with angular momentum vectors in the $\pm x$- directions. (**b**) Simulated acoustic energy fields in the cut plane, when activating IDT_1^{out} and IDT_3^{out} to generate low-frequency *x*-axis standing SAWs (left) and activating IDT_1^{out}, IDT_3^{out}, IDT_2^{mid}, and IDT_4^{mid} to generate both low-frequency *x*-axis and high-frequency *y*-axis standing SAWs (right). By comparing these two energy fields, it can be found that the potential well's *x* position does not change after introducing the *y*-axis standing SAWs.

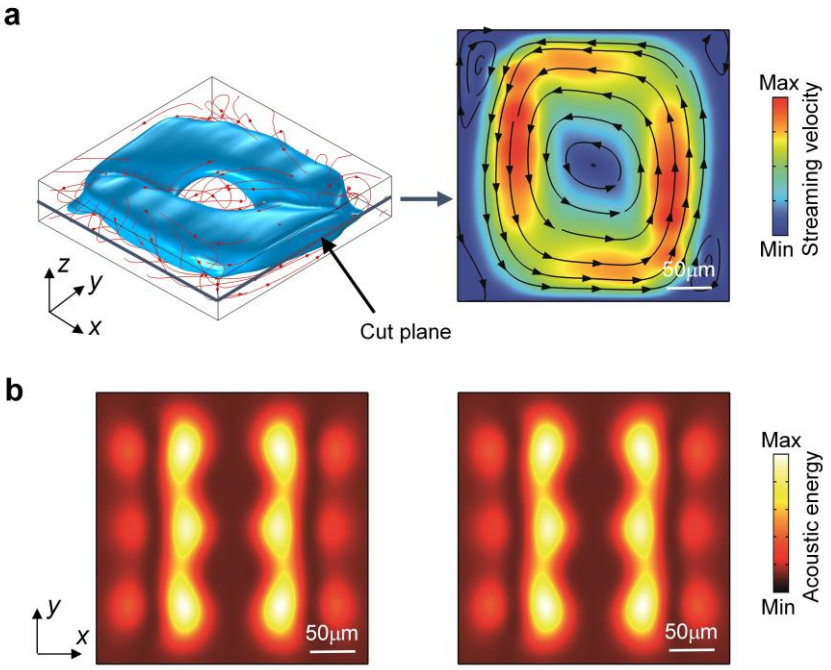

Supplementary Figure 11. Simulation results for understanding the mechanism of simultaneously translating a cell in the *x*-direction, as well as rotating the cell in the θ_z-direction. (**a**) Simulated acoustic streaming fields (left: 3D view, right: 2D view in the cut plane), when activating IDT_1^{out} and IDT_3^{out} to generate low-frequency *x*-axis standing SAWs, as well as IDT_3^{in} and IDT_7^{in} to generate high-frequency traveling SAWs. The streaming field shows a streaming vortex carrying an angular momentum that can rotate a cell in the θ_z-direction. (**b**) Simulated acoustic energy fields in the cut plane, when activating IDT_1^{out} and IDT_3^{out} (left), as well as activating IDT_1^{out}, IDT_3^{out}, IDT_3^{in}, and IDT_7^{in} (right). By comparing these two fields, it can be found that the potential well's *x* position does not change after introducing the traveling SAWs generated by IDT_3^{in} and IDT_7^{in}.

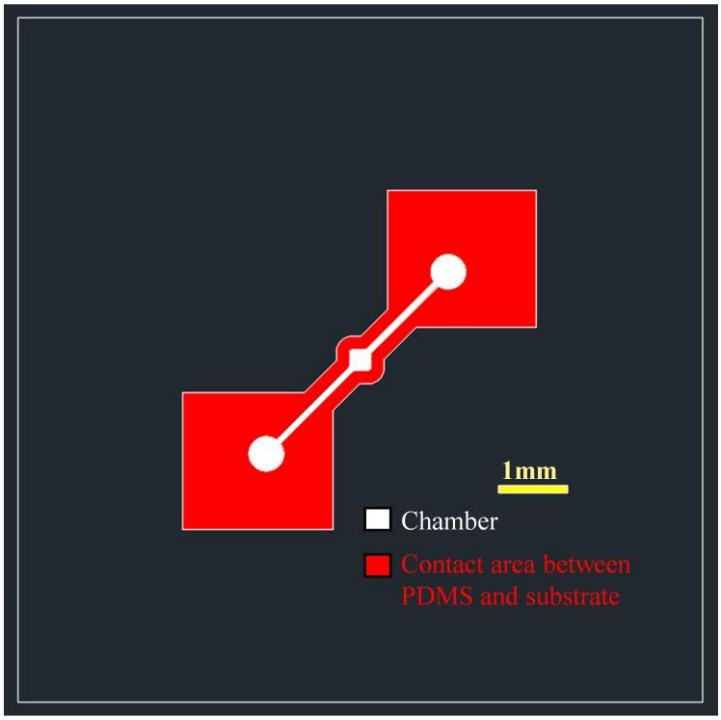

Supplementary Figure 12. Design of a microfluidic chamber of the JSAT device. Only the red region has PDMS in contact with the LiNbO3 substrate.

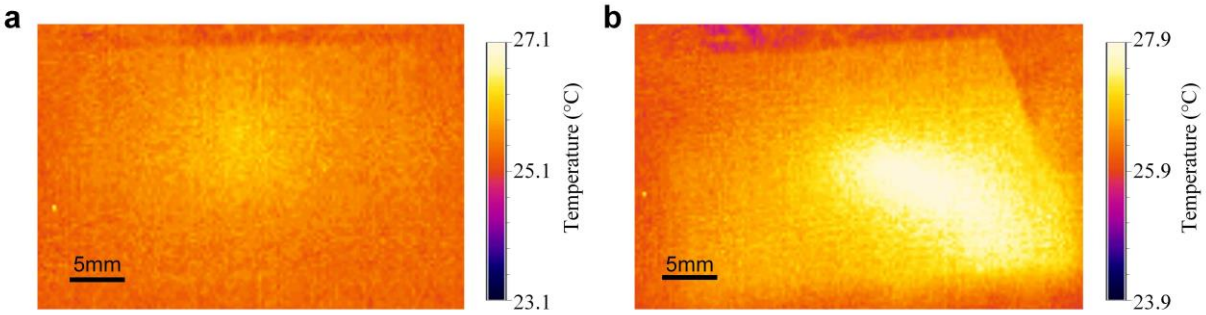

Supplementary Figure 13. Temperature fields measured from the back side of a substrate after 120 seconds. (a) Result for the case with a pair of IDTs in the middle subarray excited with a 10 Vpp input. **(b)** Result for the case with an IDT in the inner subarray excited with a 10 Vpp input. Scale bar: 5 mm.

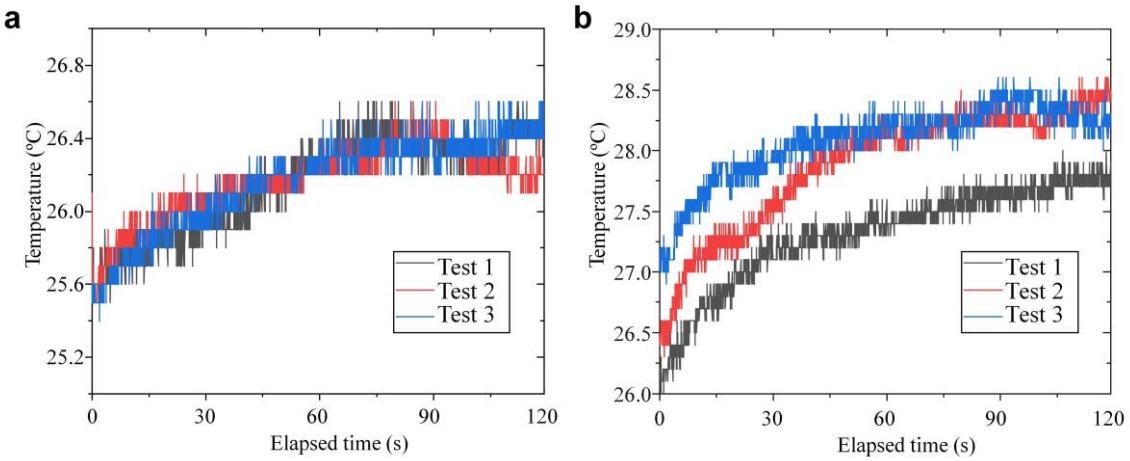

Supplementary Figure 14. Temperature change over time measured from the back side of the substrate. (a) Result for the case with a pair of IDTs in the middle subarray excited with a 10 Vpp input. **(b)** Result for the case with an IDT in the inner subarray excited with a 10 Vpp input.

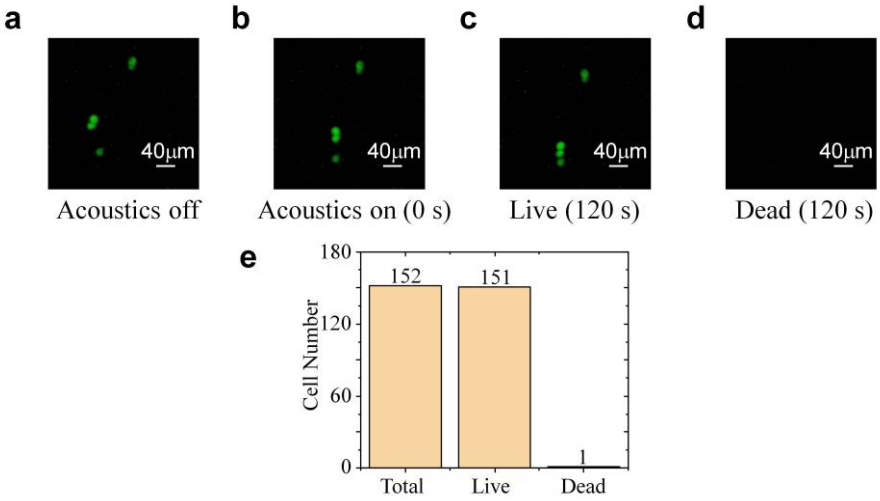

Supplementary Figure 15. Cell viability test results. (a-c) Images of the green fluorescence channel for three scenarios: **(a)** no acoustic waves applied, **(b)** acoustic waves turned on, **(c)** 120 seconds of acoustic exposure. In these images, the green dots are cells stained with calcium-AM. **(d)** Image of the red fluorescence channel. This image is black indicating no dead cells before applying acoustic waves. Before loading cells into our device, they were stained with calcium AM for revealing live cells and propidium iodide (PI) for dead cells. **(e)** Summarized cell viability data for all the N=152 cells in multiple tests (N=21). Scale bar: 40 μm.

Supplementary Note

Supplementary Note 1. Numerical simulations of acoustic pressure and radiation force

When an incident acoustic wave transmits into a bulk medium, on the basis of the perturbation theory, quantities (density ρ, pressure p, and velocity $\mathbf{v}$) used to describe the medium motion can be expressed as[1],

$$\rho=\rho_{\mathrm{f}}+\rho_1+\rho_2\,, \tag{S1a}$$

$$p=p_{\mathrm{f}}+p_1+p_2\,, \tag{S1b}$$

$$\mathbf{v}=\mathbf{0}+\mathbf{v}_1+\mathbf{v}_2\,, \tag{S1c}$$

where the first and second orders of perturbations (denoted by subscripts 1 and 2, respectively) are considered. The stationary parts representing the undisturbed properties of fluids are described by quantities with subscript f.

The acoustic radiation force $\mathbf{F}_{\mathrm{rad}}$ acting on a cell can be derived by integrating the time-averaged momentum Π transferred from acoustic waves to the cell[2],

$$\mathbf{F}_{\mathrm{rad}}=-\oiint_{s_0}\langle\Pi\rangle ds=-\oiint_{s_0}\langle p_2+\rho_{\mathrm{f}}\mathbf{v}_1\mathbf{v}_1\rangle ds\,, \tag{S2}$$

where s_0 is the cell's surface. A time-averaged quantity $\langle X\rangle$ represents the quantity X(t) averaged over a period. The time-averaged second-order pressure can be obtained with[1],

$$\langle p_2\rangle=\frac{1}{2\rho_{\mathrm{f}}c_{\mathrm{f}}^2}\langle p_1^2\rangle-\frac{1}{2}\rho_f\langle\mathbf{v}_1^2\rangle, \tag{S3}$$

where c_{f} is the pressure wave speed in the fluid medium.

As described in Eq. (S2) and (S3), the radiation force calculation needs to use $\mathbf{v}_1$ and p_1. Therefore, finite element simulations were performed using the commercial finite element software COMSOL Multiphysics, to simulate SAWs generated by the IDTs of our MDAT device, as well as the acoustic pressure and first-order velocity fields in a microfluidic chamber. The SAW substrates (Y128-cut $LiNbO_3$ wafers, thickness 0.5 mm) were all built with the piezoelectric module. Perfectly matched layers were added to the ends of the substrates to reduce the end reflections of SAWs. The liquid domain (thickness 60 μm) was modeled with the pressure acoustic physics module. The top and side boundaries of the liquid domain were set to the impedance matching condition with an impedance of

1.04 MPa s m^{-1}, consistent with the acoustic impedance of the polydimethysiloxane-based microchannel wall. An acoustic-structural coupling condition was applied to the interface between the liquid domain and the piezoelectric substrate. Each IDT was modeled with periodic electrodes, having the same width matching a quarter wavelength of the SAWs to be generated. The widths for IDTs in the outer, middle, and inner subarrays of our MDAT device were 50 μm, 25 μm, and 10 μm, respectively. By applying sinusoidal voltage excitation signals with frequencies matching the IDT resonance frequencies, the IDTs in the outer, middle, and inner subarrays can generate SAWs with wavelengths of 200 μm, 100 μm, and 40 μm, respectively. After model development, the SAW fields and acoustic pressure fields generated by our device were simulated following the frequency-domain analysis approach of COMSOL Multiphysics.

Our finite element models can output the acoustic pressure (p_1) field in the fluid domain. With this first-order pressure, the acoustic energy density E_a can be evaluated by

$$E_a = \frac{p_1^2}{4\rho_f^2 c_f^2}. \tag{S4}$$

The first-order velocity can be derived by using[3]

$$\mathbf{v}_1 = \frac{\nabla p_1}{i\rho_f \omega}, \tag{S5}$$

where ω is the angular frequency.

In order to analyze the acoustic radiation force acting on an MCF7 cell in the z-direction, our model considered a cell (radius 7.5 μm, sound speed 1490 m s^{-1}, and density 1068kg m^{-3})[4] loaded in the microfluidic chamber. The cell was modeled with the pressure acoustic physics module. The simulated acoustic pressure and first-order velocity were further used to calculate the acoustic radiation force applied to the cell with Eq. (S2).

Supplementary Note 2. Numerical simulation of acoustic streaming

The acoustic streaming in the microfluidic chamber is governed by the continuity equation and the Navier-Strokes equation[5, 6],

$$\nabla \cdot \mathbf{v}_{str} = 0, \tag{S6a}$$

$$\eta_f \nabla^2 \mathbf{v}_{str} = \nabla p_{str} - \frac{\Gamma_f \omega}{2c_f^2} \mathrm{Re}(p_1^* \mathbf{v}_1), \tag{S6b}$$

where η_f is dynamic viscosity and Γ_f is damping coefficient.

To simulate acoustic streaming in the microfluidic chamber, the creeping flow physics module was used for the liquid layer. The last term in Eq. (S6b) was the body force as a source term to activate acoustic streaming. The top, bottom, left, and right boundaries of the fluid domain were set to the boundary velocity condition ($\mathbf{v}_{str}= \mathbf{v}^{bc}$)[5, 6], where $\mathbf{v}^{bc}$ is the slip velocity and can be calculated by[6]:

$$\mathbf{n}\cdot\mathbf{v}^{bc} = 0, \tag{S7a}$$

$$(1-\mathbf{nn})\cdot\mathbf{v}^{bc} = -\frac{1}{8\omega}\nabla_{||}\left|\mathbf{v}_{1||}\right|^2 - \mathrm{Re}\left[\left(\frac{2-i}{4\omega}\nabla_{||}\cdot\mathbf{v}_{1||}^{*} + \frac{i}{2\omega}\partial_{\perp}\mathbf{v}_{1\perp}^{*}\right)\mathbf{v}_{1||}\right], \tag{S7b}$$

where $\mathbf{v}_1$ is acoustic velocity in the bulk.

The acoustofluidic streaming model was solved using a stationary solver to obtain the streaming velocity field.

Supplementary Note 3. Characterization of device temperature and cell viability

In the JSAT device, IDTs in the outer layer generate 200 μm-wavelength SAWs at 19.8 MHz (IDT_1^{out} and IDT_3^{out}) and 18.1 MHz (IDT_2^{out} and IDT_4^{out}) for translating a cell in the u_x-and u_y-directions. IDTs in the middle layer generate 100 μm-wavelength SAWs at 39.6 MHz (IDT_1^{mid} and IDT_3^{mid}) and 36.2 MHz (IDT_2^{mid} and IDT_4^{mid}) for rotating a cell in the θ_y- and θ_x-directions. Additionally, IDTs in the inner layer generate 40 μm-wavelength SAWs at 98.9 MHz (IDT_1^{in}, IDT_2^{in}, IDT_5^{in}, and IDT_6^{in}) and 95.1 MHz (IDT_3^{in}, IDT_4^{in}, IDT_7^{in}, and IDT_8^{in}) to rotate a cell in the θ_z-direction. Previously, high-frequency traveling and standing SAWs generated by IDTs were used to separate and pattern cells in microfluidic chambers[7,8], similar to our SAW devices having high-frequency IDTs and a microfluidic chamber, and they showed good cell viability[7,8].

For low-power SAW acoustic tweezers, the temperature generation is usually from the region where a PDMS chamber is bonded on the SAW substrate, as the wave energy dissipation in the PDMS significantly contributes to the temperature increase. To minimize this effect, we carefully designed our PDMS chamber by minimizing the bonding region using a design in Supplementary Figure 12. In this design, only the red region has PDMS in contact with the substrate.

We have performed temperature measurement experiments. Due to the 5 mm thick PDMS block leading to a challenge to directly measure the temperature inside a microfluidic chamber, we measured the temperature on the back side of a thin (500 μm) $LiNbO_3$ substrate with high thermal

conductivity (4-6 W/(m·K)) by using a thermal camera (Micro-epsilon/TIM400, Germany). An excitation signal with a frequency of 39.6 MHz and a voltage of 10 Vpp is applied to IDT_1^{mid} and IDT_3^{mid} in the middle layer. After 120 seconds, the temperature distribution is shown in Supplementary Figure 13a, and the temperature variation over time is depicted in Supplementary Figure 14a. The temperature change nearly stables at 120 sec with a maximum increase less than 1 °C. On the other hand, we measured the substrate temperature when exciting an inner layer IDT using a signal with a frequency of 98.9 MHz and a voltage of 10 Vpp. The temperature distribution is shown in Supplementary Figure 13b, and the corresponding temperature change over time is presented in Supplementary Figure 14b. The temperature increase was less than 2 °C. Note that these temperature measurements were performed when the bottom of the substrate was not attached to the translation stage of the microscope. When performing actual cell manipulation experiments on the microscope stage, the temperature increase should be lower, due to the heat transfer from the SAW substrate to the microscope stage. Moreover, the SAW chip can be mounted on a Peltier cooling system, as demonstrated in our previous work for temperature control[9].

We performed a cell viability test with N=152 cells. MCF7 cells were first stained with calcein-AM (C3100MP, Life Technologies) for showing live cells (green fluorescence) and propidium iodide (PI) (FP028, ABP Biosciences) for showing dead cells (red fluorescence). The cells were then injected into a microchamber and subjected to acoustic waves generated by the middle subarray's two IDTs excited by an input signal with a voltage of 10 Vpp for 120 seconds. The whole acoustic exposure process is recorded in Supplementary Movie 11. Recorded fluorescence images for a test group are given in Supplementary Figure S15a-d. We repeated the viability test procedure multiple times (N=21), as the used cell chamber only held a small number of cells. Supplementary Figure S15e summarizes the experimentally obtained cell viability data for N=152 cells, indicating a high cell viability of 99.3% after 120 seconds of acoustic exposure. Note that this viability result is obtained by calculating the ratio of cells with green fluorescence to the total number of cells. The red fluorescence emitted by PI only reveals cells that were dead before exposure to acoustic waves, as the PI staining was performed before loading the cells into our acoustic device. This PI stain could not detect cells that died as a result of acoustic exposure due to the absence of PI dye in the cell manipulation device.

For a cell stained with calcium-AM, its transition from live to dead can be revealed through the

loss of its fluorescence intensity, as the marker leaks out of the cell, a consequence of increased membrane permeability[10]. In our captured microscopic images taken at different times, nearly all cells showed no significant change in fluorescence when exposed to acoustic waves. This suggests that our acoustic tweezers do not cause significant cell damage. Numerous other studies have demonstrated that their acoustic tweezers do not result in significant cellular damage[8, 11, 12]. To gain further insights into the long-term effects of our acoustic tweezers, aspects such as the proliferation rate, DNA damage, and cell functionality still need to be characterized.

Supplementary References

1. Liang S, Chaohui W. Revised model for the radiation force exerted by standing surface acoustic waves on a rigid cylinder. *Physical Review E* **97**, 033103 (2018).
2. Liang S, Chaohui W, Qiao H. Force on a compressible sphere and the resonance of a bubble in standing surface acoustic waves. *Physical Review E* **98**, 043108 (2018).
3. Bruus H. Acoustofluidics 2: Perturbation theory and ultrasound resonance modes. *Lab on a Chip* **12**, 20-28 (2012).
4. Li P, Mao Z, Peng Z, Zhou L, Chen Y, Huang P-H, Truica CI, Drabick JJ, El-Deiry WS, Dao M, Suresh S, Huang TJ. Acoustic separation of circulating tumor cells. *Proceedings of the National Academy of Sciences* **112**, 4970 (2015).
5. Chen C, Gu Y, Philippe J, Zhang P, Bachman H, Zhang J, Mai J, Rufo J, Rawls JF, Davis EE, Katsanis N, Huang TJ. Acoustofluidic rotational tweezing enables high-speed contactless morphological phenotyping of zebrafish larvae. *Nature Communications* **12**, 1118 (2021).
6. Bruus H. 3D modeling of acoustofluidics in a liquid-filled cavity including streaming, viscous boundary layers, surrounding solids, and a piezoelectric transducer. *mathematics*, (2019).
7. Collins DJ, Khoo BL, Ma Z, Winkler A, Weser R, Schmidt H, Han J, Ai Y. Selective particle and cell capture in a continuous flow using micro-vortex acoustic streaming. *Lab on a Chip* **17**, 1769-1777 (2017).
8. Collins DJ, Morahan B, Garcia-Bustos J, Doerig C, Plebanski M, Neild A. Two-dimensional single-cell patterning with one cell per well driven by surface acoustic waves. *Nature Communications* **6**, 8686 (2015).
9. Zhao S, Wu M, Yang S, Wu Y, Gu Y, Chen C, Ye J, Xie Z, Tian Z, Bachman H, Huang P-H, Xia J, Zhang P, Zhang H, Huang TJ. A disposable acoustofluidic chip for nano/microparticle separation using unidirectional acoustic transducers. *Lab on a Chip* **20**, 1298-1308 (2020).
10. Radoškević K, de Grooth BG, Greve J. Changes in intracellular calcium concentration and pH of target cells during the cytotoxic process: A quantitative study at the single cell level. *Cytometry* **20**, 281-289 (1995).
11. Olofsson K, Carannante V, Ohlin M, Frisk T, Kushiro K, Takai M, Lundqvist A, Önfelt B, Wiklund M. Acoustic formation of multicellular tumor spheroids enabling on-chip functional and structural imaging. *Lab on a Chip* **18**, 2466-2476 (2018).
12. Baudoin M, Thomas J-L, Sahely RA, Gerbedoen J-C, Gong Z, Sivery A, Matar OB, Smagin N, Favreau P, Vlandas A. Spatially selective manipulation of cells with single-beam acoustical tweezers. *Nature Communications* **11**, 4244 (2020).